

Multi-Scale Process Modelling and Distributed Computation for Spatial Data

Andrew Zammit-Mangion*

School of Mathematics and Applied Statistics, University of Wollongong,
Wollongong, Australia

ORCID: orcid.org/0000-0002-4164-6866

Jonathan Rougier

School of Mathematics, University of Bristol, Bristol, UK

ORCID: orcid.org/0000-0003-3072-7043

Abstract

Recent years have seen a huge development in spatial modelling and prediction methodology, driven by the increased availability of remote-sensing data and the reduced cost of distributed-processing technology. It is well known that modelling and prediction using infinite-dimensional process models is not possible with large data sets, and that both approximate models and, often, approximate-inference methods, are needed. The problem of fitting simple global spatial models to large data sets has been solved through the likes of multi-resolution approximations and nearest-neighbour techniques. Here we tackle the next challenge, that of fitting complex, nonstationary, multi-scale models to large data sets. We propose doing this through the use of superpositions of spatial processes with increasing spatial scale and increasing degrees of nonstationarity. Computation is facilitated through the use of Gaussian Markov random fields and parallel Markov chain Monte Carlo based on graph colouring. The resulting model allows for both distributed computing and distributed data. Importantly, it provides opportunities for genuine model and data scalability and yet is still able to borrow strength across large spatial scales. We illustrate a two-scale version on a data set of sea-surface temperature containing on the order of one million observations, and compare our approach to state-of-the-art spatial modelling and prediction methods.

Keywords: Graph Colouring, Markov Chain Monte Carlo, Parallel Sampling, Spatial Statistics

1 Introduction

Large spatial/spatio-temporal data sets are now centre-stage in several of the environmental sciences such as meteorology and glaciology. The two fundamental tools available to the spatial statistician to deal with such data are the hierarchical model and the closely-related notion of conditional independence (Cressie and Wikle, 2011, Section 2.1.5). In a two layer, linear, Gaussian, data-process model, the widely adopted assumption that

*Corresponding author: Tel.: +61-2-4221-5112; E-mail: azm@uow.edu.au

data are conditionally independent, given the underlying process, is sufficient for developing inferential algorithms that scale linearly with the dimension of the data. Several methods capitalise on this approach for the spatial or spatio-temporal analysis of big data; these include fixed rank kriging (Cressie and Johannesson, 2008), predictive processes (Banerjee et al., 2008), the use of nearest neighbours (Datta et al., 2016), and a suite of approaches based on Gaussian Markov random field (GMRF) approximations to geostatistical models (e.g., Rue and Tjelmeland, 2002; Lindgren et al., 2011; Nychka et al., 2015). For spatio-temporal variants see, for example, Sahu and Mardia (2005); Dewar et al. (2009); Cressie and Wikle (2011) and Wikle et al. (2019).

Shifting the computational burden from the upper, data layer to the second, process layer is only beneficial if the computations associated with the second layer are tractable. Consequently, finite-dimensional assumptions are often made for the model within this layer. Dimensionality reduction needs to be done with care, as the space of the latent functions that can be reproduced is no larger than the span of the set of basis functions used for dimensionality reduction. If this space does not contain the true signal, then any residual observed signal variability will be, at best, attributed to other components in the hierarchical model, typically measurement error or fine-scale process variability. At worst, there is no such component and inferences are over-confident (e.g., Zammit-Mangion and Cressie, 2019). As such, low-dimensional models are only able to give reliable inferences in a big data scenario if it is known, prior to an analysis, that the data is a noisy version of a signal that is a member of the (rather small) latent space being considered.

As a result, model approximations have been developed that ensure that several basis functions can be used. Two popular ones include one based on multi-scale GMRFs (Nychka et al., 2015), and one based on a multi-resolution approximation to the process covariance function (Katzfuss, 2017). Unfortunately, models based on multi-scale GMRFs are currently hindered by the computational bottleneck of the required sparse Cholesky factorisations, while neither approach is well-suited to approximate highly nonstationary multi-scale processes. Rather, their motivation, and the associated inference methods that have been designed for them, are built on the premise that the underlying covariance function of the process is relatively simple; the approximations are made to be able to fit the model and predict with it when using large data sets. These methods work very well when this is indeed the case. The next challenge is therefore to use models and appropriate inference methods for when we have big data *and* for when the underlying process is multi-scale and highly nonstationary, as it is indeed the case in several environmental applications.

The model we propose in Section 2 models the process $Y(\cdot)$ as a sum of several processes at various scales, where the degree of nonstationarity increases with the scale of the process. We approximate these processes using GMRFs so that the conditional dependence structure of the latent variables can be exploited for local processing and the use of a parallel Gibbs sampler, as discussed in Section 3. In Section 4 we give some practical guidelines on how to construct the model, and in Section 5 we demonstrate the two-scale variant on a data set containing on the order of one million observations using around one million basis functions, with the covariances constructed through several hundreds of parameters to allow for local nonstationarity. Section 6 concludes.

2 Multi-scale nonstationary spatial processes

In this section we detail the model through its hierarchical structure, adopting the terminology of Berliner (1996). The top layer in the hierarchy is the data model (Section 2.1), the middle layer is the process model (Section 2.2), and the bottom layer is the parameter model (Section 2.3). We denote subsets of vectors and matrices through superscripts. Specifically, for a vector \mathbf{X} , \mathbf{X}^{I_1} denotes the sub-vector of \mathbf{X} constructed from the elements with indices in the set I_1 . For a matrix \mathbf{A} , \mathbf{A}^{I_1} denotes the sub-matrix of \mathbf{A} constructed by taking the rows with indices in I_1 , while \mathbf{A}^{I_1, I_2} is constructed by taking the rows with indices in I_1 and columns with indices in I_2 .

2.1 Data model

Assume one has observations $\mathbf{Z} \equiv (Z_1, \dots, Z_m)^\top$ of some underlying zero-mean spatial process $Y(\cdot)$ on $D \subset \mathbb{R}^2$ or $D \subseteq \mathbb{S}^2$. Our data model is given by $Z_l = Y(\mathbf{s}_l) + \varepsilon_l$, for $l = 1, \dots, m$, where ε_l is Gaussian measurement-error with variance $\sigma_\varepsilon^2(\mathbf{s}_l)$ and $D^o \equiv \{\mathbf{s}_1, \dots, \mathbf{s}_m\} \subset D$ is a set of point-referenced measurement locations. In this article we assume that $\{\varepsilon_l\}$ are uncorrelated conditional on $\sigma_\varepsilon^2(\cdot)$, and that \mathbf{Z} is large; in our case study in Section 5, m is on the order of one million.

2.2 Process model

We define $Y(\cdot)$ to be the sum of $(K + 1)$ independent Gaussian processes (GPs), $Y(\cdot) = Y_0(\cdot) + \sum_{k=1}^K Y_k(\cdot)$, where $Y_0(\cdot)$ is stationary with large spatial scales, and $Y_k(\cdot)$ is nonstationary with spatial scale decreasing with increasing k . Without loss of generality we assume that $Y_k(\cdot), k = 0, \dots, K$, have zero expectation. We model the GPs through the stochastic partial differential equations

$$(\kappa_0^2 - \Delta)^{\alpha_0/2}(\tau_0 Y_0(\mathbf{s})) = W_0(\mathbf{s}), \quad \mathbf{s} \in D, \quad (1)$$

$$(\kappa_k(\mathbf{s})^2 - \Delta)^{\alpha_k/2}(\tau_k(\mathbf{s})Y_k(\mathbf{s})) = W_k(\mathbf{s}), \quad \mathbf{s} \in D, \quad k = 1, \dots, K, \quad (2)$$

where $W_k(\cdot), k = 0, \dots, K$, are Gaussian spatial white noise processes, κ_k are spatial scale parameters, τ_k control the process variance, and Δ is the Laplacian. When $D \subset \mathbb{R}^2$ the solution to (1) is a stationary GP with Matérn covariance function with smoothness parameter $\nu_0 = \alpha_0 - 1$, while that to (2) is a nonstationary process that, under some regularity assumptions on $\kappa_k(\cdot)$ and $\tau_k(\cdot)$, exhibits local stationary Matérn behaviour with smoothness parameter $\nu_k = \alpha_k - 1$. As in Lindgren et al. (2011) and Lindgren and Rue (2015) we project $Y_k(\cdot), k = 0, 1, \dots, K$, onto a finite-dimensional basis through $Y_k(\cdot) = \mathbf{a}_k(\cdot)^\top \boldsymbol{\eta}_k$, where $\mathbf{a}_k(\cdot)$ is a vector of r_{η_k} tent basis functions on a triangulation of D , T_{η_k} say, and $\boldsymbol{\eta}_k \sim \text{Gau}(\mathbf{0}, \mathbf{Q}_k^{-1})$, where \mathbf{Q}_k is a sparse precision matrix. The coefficients $\boldsymbol{\eta}_k, k = 0, \dots, K$, can be associated with the vertices of the basis functions they weight; this property will facilitate graph partitioning and colouring in Section 3.

After projecting onto our finite-dimensional subspace, we can write

$$\mathbf{Z} = \sum_{k=0}^K \mathbf{A}_k \boldsymbol{\eta}_k + \boldsymbol{\varepsilon},$$

where $\mathbf{A}_k \equiv (\mathbf{a}_k(\mathbf{s}_l) : l = 1, \dots, m)^\top$, $\boldsymbol{\varepsilon} \sim \text{Gau}(\mathbf{0}, \mathbf{Q}_\varepsilon^{-1})$, and \mathbf{Q}_ε is diagonal with measurement-error precisions as non-zero elements. Collect all unknown model parameters (see Section 2.3) into the vector $\boldsymbol{\theta}$. Let $\mathbf{A} \equiv (\mathbf{A}_0, \dots, \mathbf{A}_K)$, $\mathbf{Q} \equiv \text{bdiag}(\mathbf{Q}_0, \dots, \mathbf{Q}_K)$

and $\boldsymbol{\eta} \equiv (\boldsymbol{\eta}_0^\top, \dots, \boldsymbol{\eta}_K^\top)^\top$. For this model, which is structurally identical to the LatticeKrig model (Nychka et al., 2015), $\text{prec}(\boldsymbol{\eta} \mid \mathbf{Z}, \boldsymbol{\theta}) \equiv \tilde{\mathbf{Q}} = \mathbf{A}^\top \mathbf{Q}_\varepsilon \mathbf{A} + \mathbf{Q}$ and $\tilde{\mathbf{Q}}\tilde{\boldsymbol{\mu}} = \mathbf{A}^\top \mathbf{Q}_\varepsilon \mathbf{Z}$, where $\tilde{\boldsymbol{\mu}} \equiv \mathbb{E}(\boldsymbol{\eta} \mid \mathbf{Z}, \boldsymbol{\theta})$. As the data \mathbf{Z} are point-referenced, $\boldsymbol{\eta} \mid \mathbf{Z}, \boldsymbol{\theta}$ is also a GMRF since $\tilde{\mathbf{Q}}$ is also sparse (since \mathbf{A} has sparse rows and \mathbf{Q}_ε is diagonal). However, both \mathbf{Z} and $\boldsymbol{\eta}$ can contain millions of elements so that storing, let alone computing with, $\tilde{\mathbf{Q}}$ and \mathbf{A} can become impractical. On the other hand GMRFs have the desirable property that they admit parallel-data and parallel-model conditional structures which can be used to facilitate computation. More details on how we exploit this property are given in Section 3.

2.3 Parameter model

As in Lindgren and Rue (2015) we do not consider the natural parameters $\tau_k, \kappa_k, k = 0, 1, \dots, K$, directly. Rather, we construct a parameter model for the latent process standard deviation σ_k and range ρ_k , which in our setting are related to the natural parameters through

$$\begin{aligned} \log \tau_k &= \frac{1}{2} \log \left(\frac{\Gamma(\nu_k)}{4\pi \Gamma(\alpha_k)} \right) - \log \sigma_k - \nu_k \log \kappa_k, \\ \log \kappa_k &= \frac{1}{2} \log (8\nu_k) - \log \rho_k, \end{aligned}$$

where $\Gamma(\cdot)$ is the gamma function. Throughout, we assume that $\nu_k, k = 0, \dots, K$, is known.

We decompose the spatially-varying parameter $\sigma_\varepsilon(\cdot)$ as a weighted sum of r_ε basis functions $\mathbf{b}_\varepsilon(\cdot)$ constructed over a triangulation T_ε on D . We also decompose $\sigma_k(\cdot)$ and $\rho_k(\cdot), k = 1, \dots, K$, as weighted sums of r_{θ_k} basis functions, $\mathbf{b}_k(\cdot)$, constructed over a triangulation T_{θ_k} on D . The triangulation T_{θ_k} will generally be much coarser than T_{η_k} . These decompositions yield the following parameter models,

$$\sigma_\varepsilon(\cdot) = \mathbf{b}_\varepsilon(\cdot)^\top \boldsymbol{\theta}_\varepsilon, \quad \sigma_k(\cdot) = \mathbf{b}_k(\cdot)^\top \boldsymbol{\theta}_{\sigma_k}, \quad \rho_k(\cdot) = \mathbf{b}_k(\cdot)^\top \boldsymbol{\theta}_{\rho_k},$$

for $k = 1, \dots, K$.

We assume that the elements of the parameter vector $\boldsymbol{\theta}_X, X \in \{\varepsilon, \sigma_1, \rho_1, \dots, \sigma_K, \rho_K\}$, are distributed according to a lognormal (LN) distribution. That is, we let

$$\boldsymbol{\theta}_X^{\{i\}} \mid \omega_X, \lambda_X \stackrel{\text{iid}}{\sim} \text{LN}(\omega_X, \lambda_X), \quad i = 1, \dots, r_X, \quad (3)$$

where $\omega_X = \mathbb{E}(\log(\boldsymbol{\theta}_X^{\{i\}}))$ and $\lambda_X = \text{var}(\log(\boldsymbol{\theta}_X^{\{i\}}))$. The hyperparameters ω_{ρ_k} and λ_{ρ_k} need to reflect a prior judgement that the process range decreases with increasing k ; we provide some guidelines in Section 4 and an example of how this can be done in practice with a two-scale process in Section 5. Appropriate hyperparameters for constructing the prior distributions over $\boldsymbol{\theta}_\varepsilon$ and $\boldsymbol{\theta}_{\sigma_k}$ can usually be deduced from exploratory data analysis.

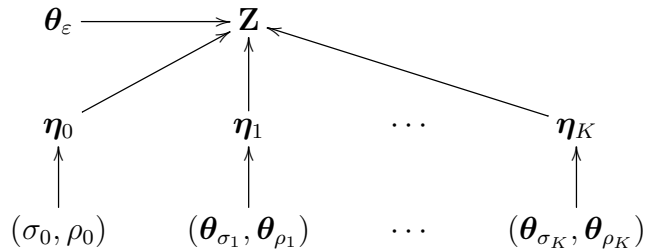
We complete our parameter model by equipping the parameters appearing in the coarse component, ρ_0 and σ_0 , with the prior lognormal distributions

$$\sigma_0 \sim \text{LN}(\omega_{\sigma_0}, \lambda_{\sigma_0}), \quad (4)$$

$$\rho_0 \sim \text{LN}(\omega_{\rho_0}, \lambda_{\rho_0}), \quad (5)$$

where reasonable values of ω_{σ_0} and λ_{σ_0} can generally be deduced from exploratory analysis of the data, while ω_{ρ_0} and λ_{ρ_0} can generally be fixed using prior application knowledge (see Sections 4 and 5).

To summarise, the full set of parameters and the full conditional dependence structure of our model is given by the following directed acyclic graph (DAG):



The coefficients $\boldsymbol{\eta}_0$ construct a stationary process with spatially-invariant standard deviation and range, σ_0 and ρ_0 , respectively. On the other hand, $\boldsymbol{\eta}_1, \dots, \boldsymbol{\eta}_K$ construct nonstationary processes with spatially-varying standard deviations and ranges. For these nonstationary processes the standard deviations and ranges are modelled through the coefficients $\{\boldsymbol{\theta}_{\sigma_k}\}$ and $\{\boldsymbol{\theta}_{\rho_k}\}$, where the individual elements are independent and their marginal distributions are pre-specified. The measurement errors $\boldsymbol{\varepsilon}$ are assumed to be spatially uncorrelated and are thus modelled using just the variance coefficients, $\boldsymbol{\theta}_\varepsilon$.

3 Inference

The value of this model is partly that it provides a flexible representation of spatial nonstationarity, and partly that it can be updated by conditioning in a serial fashion using many Gibbs steps. Additionally, the Gibbs steps for $\boldsymbol{\eta}_k$ and $\boldsymbol{\theta}_k \equiv (\boldsymbol{\theta}_{\sigma_k}^\top, \boldsymbol{\theta}_{\rho_k}^\top)^\top$, $k = 1, \dots, K$, can be split and parallelised if they are too difficult to sample directly. We hence have a parallel MCMC scheme that can scale well with both data size and model complexity.

In Section 3.1 we discuss Gibbs sampler updates for the process and parameter coefficients in the first scale; in Section 3.2 the updates for the process and parameter coefficients in the other scales; in Section 3.3 a re-updating strategy for the process coefficients for $k > 0$; in Section 3.4 the updates for the measurement-error variance parameters; and in Section 3.5 we summarise the sampler.

3.1 Updating the process and parameter coefficients for scale $k = 0$

Since $\boldsymbol{\theta}_0 \equiv (\sigma_0, \rho_0)^\top$ and $\boldsymbol{\eta}_0$ can be expected to be highly correlated a posteriori (Knorr-Held and Rue, 2002) we sample them jointly in the Gibbs sampler, which substantially improves the mixing of the Markov chains. Specifically, we sample from the full conditional distribution

$$\text{pr}(\boldsymbol{\eta}_0 \mid \boldsymbol{\theta}_0, \text{eelse}) \text{pr}(\boldsymbol{\theta}_0 \mid \text{eelse excl. } \boldsymbol{\eta}_0), \quad (6)$$

by first sampling from $\text{pr}(\boldsymbol{\theta}_0 \mid \text{eelse excl. } \boldsymbol{\eta}_0)$ and subsequently from $\text{pr}(\boldsymbol{\eta}_0 \mid \boldsymbol{\theta}_0, \text{eelse})$, where we use ‘eelse’ as shorthand for ‘everything else.’ Here, and in the rest of the article, we always sample using the most recently sampled values of the other variables.

The conditional distribution of $\boldsymbol{\theta}_0$ in (6) is a partially collapsed distribution, where $\boldsymbol{\eta}_0$ is integrated out:

$$\begin{aligned} \text{pr}(\boldsymbol{\theta}_0 \mid \text{eelse excl. } \boldsymbol{\eta}_0) &= \int \text{pr}(\boldsymbol{\eta}_0, \boldsymbol{\theta}_0 \mid \text{eelse}) \, \text{d}\boldsymbol{\eta}_0 \\ &\propto \int \text{pr}(\mathbf{Z} \mid \boldsymbol{\eta}_0, \text{eelse}) \text{pr}(\boldsymbol{\eta}_0 \mid \boldsymbol{\theta}_0) \, \text{d}\boldsymbol{\eta}_0 \text{pr}(\boldsymbol{\theta}_0). \end{aligned} \quad (7)$$

The integrand in this distribution is Gaussian and therefore the integration can be evaluated analytically to give

$$\begin{aligned} \log \text{pr}(\boldsymbol{\theta}_0 \mid \text{eelse excl. } \boldsymbol{\eta}_0) &= \frac{1}{2} \log |\mathbf{Q}_\varepsilon| + \frac{1}{2} \log |\mathbf{Q}_0| - \frac{1}{2} \log |\tilde{\mathbf{Q}}_0| - \frac{1}{2} \tilde{\mathbf{Z}}^\top \mathbf{Q}_\varepsilon \tilde{\mathbf{Z}} + \\ &\quad \frac{1}{2} \tilde{\mathbf{Z}}^\top \mathbf{Q}_\varepsilon \mathbf{A}_0^\top \tilde{\boldsymbol{\mu}}_0 + \log \text{pr}(\boldsymbol{\theta}_0) + \text{const.}, \end{aligned} \quad (8)$$

where $\tilde{\mathbf{Q}}_0 = \mathbf{A}_0^\top \mathbf{Q}_\varepsilon \mathbf{A}_0 + \mathbf{Q}_0$, $\tilde{\boldsymbol{\mu}}_0 = \tilde{\mathbf{Q}}_0^{-1} \mathbf{A}_0^\top \mathbf{Q}_\varepsilon \tilde{\mathbf{Z}}$ and $\tilde{\mathbf{Z}} = \mathbf{Z} - \sum_{k>0} \mathbf{A}_k \boldsymbol{\eta}_k$. Since $Y_0(\cdot)$ captures large scales, T_{η_0} can be made sufficiently coarse so that factorising \mathbf{Q}_0 , as well as algebraic operations of the form $\tilde{\mathbf{Q}}_0^{-1} \mathbf{X} = \mathbf{Y}$, can be done on a single computing node. We provide more detailed guidelines on this in Section 4. All other operations can be computed in a distributed fashion from sums and product of smaller vectors and matrices corresponding to chunks of \mathbf{Z} , $\{\mathbf{A}_k\}$, and $\{\boldsymbol{\eta}_k\}$. There is therefore no theoretical limit on the data size and number of scales K that will preclude sampling from this distribution in a reasonable time frame given sufficient parallel computing resources. This is also true for all the sampling operations we outline below. The conditional distribution (8) does not have a recognisable distribution in $\boldsymbol{\theta}_0$, and so this update uses a Metropolis-Hastings step.

After updating $\boldsymbol{\theta}_0$ we update $\boldsymbol{\eta}_0$. The full conditional distribution of $\boldsymbol{\eta}_0$ is given by

$$\boldsymbol{\eta}_0 \mid \text{eelse} \sim \text{Gau}(\tilde{\boldsymbol{\mu}}_0, \tilde{\mathbf{Q}}_0^{-1}), \quad (9)$$

where note that $\tilde{\boldsymbol{\mu}}_0$ and $\tilde{\mathbf{Q}}_0$ are also required to compute (8). A sample of (9) is therefore obtained ‘for free’ after the update of $\boldsymbol{\theta}_0$.

3.2 Updating the process and parameter coefficients for scale $k = 1, \dots, K$

The update for $\boldsymbol{\theta}_k \equiv (\boldsymbol{\theta}_{\sigma_k}^\top, \boldsymbol{\theta}_{\rho_k}^\top)^\top$ is more tricky than that of $\boldsymbol{\theta}_0$: The full conditional distribution for $\boldsymbol{\theta}_k$ has the same structure as that for $\boldsymbol{\theta}_0$ given in (7), but since for $k > 0$ the triangulation T_{η_k} is fine and r_{η_k} is large, the integrand cannot be evaluated in memory, and so a sequential strategy is necessary.

Let \mathcal{I} index one element of $\boldsymbol{\theta}_{\sigma_k}$ (equivalently $\boldsymbol{\theta}_{\rho_k}$) and, with a slight abuse of notation, let $\boldsymbol{\theta}_k^\mathcal{I}$ denote the pair of elements $(\boldsymbol{\theta}_{\sigma_k}^\mathcal{I}, \boldsymbol{\theta}_{\rho_k}^\mathcal{I})^\top$. Let the set \mathcal{T} be the *effective process footprint* of $\boldsymbol{\theta}_k^\mathcal{I}$, defined as the set of indices of $\boldsymbol{\eta}_k$ for which the (prior) conditional distribution of $\boldsymbol{\eta}_k^{\text{rest}}$ *excluding* $\boldsymbol{\eta}_k^\mathcal{I}$ is approximately independent of $\boldsymbol{\theta}_k^\mathcal{I}$. It might be helpful to picture $\boldsymbol{\eta}_k^\mathcal{I}$ as a ‘halo’ around $\text{supp}(\mathbf{b}_k^\mathcal{I})$, where $\text{supp}(\cdot)$ denotes a function’s support. Further, let \mathcal{F} be the *data footprint* of $\boldsymbol{\eta}_k^\mathcal{I}$, that is, the set of indices of the data points that lie in the subset of the domain given by $\cup_{i \in \mathcal{T}} \text{supp}(\mathbf{a}_k^{\{i\}})$. Under the partitioning of

the coefficients $\{\boldsymbol{\theta}_k^{\mathcal{I}}, \boldsymbol{\theta}_k^{\text{rest}}\}$, $\{\boldsymbol{\eta}_k^{\mathcal{I}}, \boldsymbol{\eta}_k^{\text{rest}}\}$, and the data $\{\mathbf{Z}^{\mathcal{F}}, \mathbf{Z}^{\text{rest}}\}$, the relevant part of the full DAG is



where we have used a dashed line to denote a conditional dependence relationship that is weak, and one that can potentially be ignored for practical purposes.

We jointly update $(\boldsymbol{\eta}_k^{\mathcal{I}}, \boldsymbol{\theta}_k^{\mathcal{I}})$ via the full conditional distribution

$$\text{pr}(\boldsymbol{\eta}_k^{\mathcal{I}}, \boldsymbol{\theta}_k^{\mathcal{I}} \mid \text{eelse}) = \text{pr}(\boldsymbol{\eta}_k^{\mathcal{I}} \mid \boldsymbol{\theta}_k^{\mathcal{I}}, \text{eelse}) \text{pr}(\boldsymbol{\theta}_k^{\mathcal{I}} \mid \text{eelse excl. } \boldsymbol{\eta}_k^{\mathcal{I}}),$$

by first sampling from $\text{pr}(\boldsymbol{\theta}_k^{\mathcal{I}} \mid \text{eelse excl. } \boldsymbol{\eta}_k^{\mathcal{I}})$ and subsequently from $\text{pr}(\boldsymbol{\eta}_k^{\mathcal{I}} \mid \boldsymbol{\theta}_k^{\mathcal{I}}, \text{eelse})$. As with $\boldsymbol{\theta}_0$ we have that $\text{pr}(\boldsymbol{\theta}_k^{\mathcal{I}} \mid \text{eelse excl. } \boldsymbol{\eta}_k^{\mathcal{I}})$ is a partially collapsed distribution given by

$$\begin{aligned} \text{pr}(\boldsymbol{\theta}_k^{\mathcal{I}} \mid \text{eelse excl. } \boldsymbol{\eta}_k^{\mathcal{I}}) &= \int \text{pr}(\boldsymbol{\theta}_k^{\mathcal{I}}, \boldsymbol{\eta}_k^{\mathcal{I}} \mid \text{eelse}) \, \text{d}\boldsymbol{\eta}_k^{\mathcal{I}} \\ &\propto \int \text{pr}(\mathbf{Z}^{\mathcal{F}} \mid \boldsymbol{\eta}_k^{\mathcal{I}}, \text{eelse}) \text{pr}(\boldsymbol{\eta}_k^{\mathcal{I}} \mid \boldsymbol{\eta}_k^{\text{rest}}, \boldsymbol{\theta}_k^{\mathcal{I}}, \boldsymbol{\theta}_k^{\text{rest}}) \\ &\quad \times \text{pr}(\boldsymbol{\eta}_k^{\text{rest}} \mid \boldsymbol{\theta}_k^{\mathcal{I}}, \boldsymbol{\theta}_k^{\text{rest}}) \, \text{d}\boldsymbol{\eta}_k^{\mathcal{I}} \text{pr}(\boldsymbol{\theta}_k^{\mathcal{I}}). \end{aligned}$$

Since $\boldsymbol{\eta}_k$ is a Gaussian Markov random field it is computationally cheap to evaluate the conditional distribution $\text{pr}(\boldsymbol{\eta}_k^{\mathcal{I}} \mid \boldsymbol{\eta}_k^{\text{rest}}, \boldsymbol{\theta}_k^{\mathcal{I}}, \boldsymbol{\theta}_k^{\text{rest}})$, but it is computationally expensive to evaluate the ‘marginal’ distribution $\text{pr}(\boldsymbol{\eta}_k^{\text{rest}} \mid \boldsymbol{\theta}_k^{\mathcal{I}}, \boldsymbol{\theta}_k^{\text{rest}})$, as is required for this update. We therefore resort to the approximation implied by the dashed line of the DAG in (10),

$$\text{pr}(\boldsymbol{\eta}_k^{\text{rest}} \mid \boldsymbol{\theta}_k^{\mathcal{I}}, \boldsymbol{\theta}_k^{\text{rest}}) \approx \text{pr}(\boldsymbol{\eta}_k^{\text{rest}} \mid \tilde{\boldsymbol{\theta}}_k^{\mathcal{I}}, \boldsymbol{\theta}_k^{\text{rest}}), \quad (11)$$

where we have replaced $\boldsymbol{\theta}_k^{\mathcal{I}}$ by some value $\tilde{\boldsymbol{\theta}}_k^{\mathcal{I}}$, which may depend on the value of $\boldsymbol{\theta}_k^{\text{rest}}$. This approximation is motivated by the fact that, notionally, $\boldsymbol{\theta}_k^{\mathcal{I}}$ controls the variance parameters $\sigma_k(\cdot)$ and $\rho_k(\cdot)$ *locally*, and can therefore be expected to have diminishing effect on the probability of $\boldsymbol{\eta}_k^{\text{rest}}$ by the marginalisation property of the Gaussian distribution. An attractive feature of this approximation is that it can be improved as much as needed, at the expense of increased computational cost, by increasing the size of the effective process footprint \mathcal{T} . The chosen effective process footprint should be one for which the approximation (11) is acceptable in practice. In our application, setting \mathcal{T} to be the indices of the basis functions $\mathbf{a}_k(\cdot)$ that have their and their neighbours’ maxima inside $\text{supp}(\mathbf{b}_k^{\mathcal{I}})$ sufficed, but more conservative choices could be considered if needed; see Section 4.

Our approximation yields

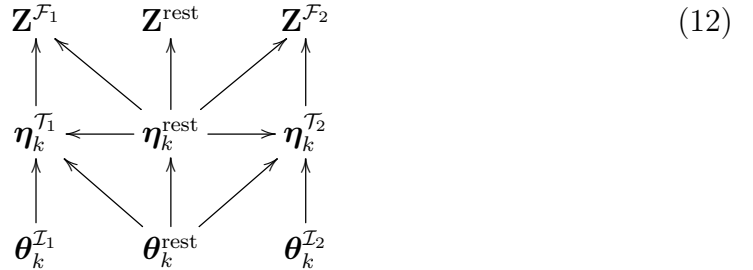
$$\text{pr}(\boldsymbol{\theta}_k^{\mathcal{I}} \mid \text{eelse excl. } \boldsymbol{\eta}_k^{\mathcal{I}}) \propto \int \text{pr}(\mathbf{Z}^{\mathcal{F}} \mid \boldsymbol{\eta}_k^{\mathcal{I}}, \text{eelse}) \text{pr}(\boldsymbol{\eta}_k^{\mathcal{I}} \mid \boldsymbol{\eta}_k^{\text{rest}}, \boldsymbol{\theta}_k^{\mathcal{I}}, \boldsymbol{\theta}_k^{\text{rest}}) \, \text{d}\boldsymbol{\eta}_k^{\mathcal{I}} \text{pr}(\boldsymbol{\theta}_k^{\mathcal{I}}),$$

the log of which is identical in structure to (8) with an added term due to the presence of $\boldsymbol{\eta}_k^{\text{rest}}$ in the conditional distribution of $\boldsymbol{\eta}_k^{\mathcal{I}}$ (Rue and Held, 2005, Section 2.2.5). This

extra term does not alter the computational or memory complexity of the operations. Therefore, the computations will be tractable as long as $|\mathcal{T}|$ is on the same order of magnitude as r_{η_0} , which we have set to be sufficiently small to make it possible for these computations to be done on a single computing node.

As with θ_0 , this distribution has no recognisable form and requires a Metropolis-Hastings step. Further, the computations for this conditional distribution can once again benefit from a distributed data framework. However, since there are r_{θ_k} of them (one for each parameter basis function), for the inference framework to be scalable the computational time required by these updates must not depend on r_{θ_k} . This is indeed the case under our approximation as we now show.

Take two sets of parameters $\theta_k^{\mathcal{I}_1}$ and $\theta_k^{\mathcal{I}_2}$ with associated effective process footprints \mathcal{T}_1 and \mathcal{T}_2 for which $\eta_k^{\mathcal{T}_1} \perp\!\!\!\perp \eta_k^{\mathcal{T}_2} \mid \eta_k^{\text{rest}}, \theta_k$ and for which the associated data footprints $\mathcal{F}_1 \cap \mathcal{F}_2 = \emptyset$ (this condition is trivially satisfied in our context where \mathbf{Z} are point referenced and the $\{\mathbf{a}_k(\cdot)\}$ are tent basis functions). Partition θ_k as $\{\theta_k^{\mathcal{I}_1}, \theta_k^{\mathcal{I}_2}, \theta_k^{\text{rest}}\}$, η_k as $\{\eta_k^{\mathcal{T}_1}, \eta_k^{\mathcal{T}_2}, \eta_k^{\text{rest}}\}$, and \mathbf{Z} as $\{\mathbf{Z}^{\mathcal{F}_1}, \mathbf{Z}^{\mathcal{F}_2}, \mathbf{Z}^{\text{rest}}\}$. Then the relevant part of the DAG where we now omit the weak conditional dependencies for clarity, is



From the moralised version of (12), we immediately see that the coefficients $\{\eta_k^{\text{rest}}, \theta_k^{\text{rest}}\}$ separate the two groups $\{\eta_k^{\mathcal{T}_1}, \theta_k^{\mathcal{I}_1}\}$ and $\{\eta_k^{\mathcal{T}_2}, \theta_k^{\mathcal{I}_2}\}$ so that

$$\begin{aligned} \text{pr}(\{\eta_k^{\mathcal{T}_1}, \theta_k^{\mathcal{I}_1}\}, \{\eta_k^{\mathcal{T}_2}, \theta_k^{\mathcal{I}_2}\} \mid \text{eelse}) &\propto \text{pr}(\eta_k^{\mathcal{T}_1}, \theta_k^{\mathcal{I}_1} \mid \text{eelse}) \text{pr}(\eta_k^{\mathcal{T}_2}, \theta_k^{\mathcal{I}_2} \mid \text{eelse}) \\ &= \text{pr}(\eta_k^{\mathcal{T}_1} \mid \text{eelse}) \text{pr}(\theta_k^{\mathcal{I}_1} \mid \text{eelse excl. } \eta_k^{\mathcal{T}_1}) \\ &\quad \times \text{pr}(\eta_k^{\mathcal{T}_2} \mid \text{eelse}) \text{pr}(\theta_k^{\mathcal{I}_2} \mid \text{eelse excl. } \eta_k^{\mathcal{T}_2}). \end{aligned} \quad (13)$$

Therefore the update operations for $\theta_k^{\mathcal{I}_1}$ and $\theta_k^{\mathcal{I}_2}$ can be dispatched to different cores in a multicore computing architecture, and the updates can be done in parallel. We can identify the sets of parameters that can be updated in parallel by *colouring* the full conditional dependency graph of θ_k under our chosen set of effective footprints, such that no conditionally dependent elements of θ_k have the same colour. In a minimal setting, where we choose the effective process footprints as the subset of η_k for which the maxima of the associated basis functions and those of its Markov blanket lie in the support of $\mathbf{b}_k^{\mathcal{I}}$, the conditional dependency graph is the edge-preserving bijection of the spatial graph T_{θ_k} . We can therefore make use of the four-colour theorem (Gonthier, 2008) so that a sample of θ_k can be done in exactly four steps, irrespective of the scale or data size. More conservative choices on the footprints will result in the use of more colours, and hence a lower degree of parallelisation, but still the number of colours will be independent of scale and data size, rendering this model and inferential technique scalable. In our application we made use of the backtracking algorithm for colouring the graph (Bender and Wilf, 1985).

Consider now the joint update of a single footprint and parameter $(\eta_k^{\mathcal{T}}, \theta_k^{\mathcal{I}})$. As in the joint update of (η_0, θ_0) , a sample from the full conditional distribution of $\eta_k^{\mathcal{T}}$ is obtained

‘for free’ since it is Gaussian with a mean vector and a precision matrix that are also used when sampling $\boldsymbol{\theta}_k^{\mathcal{I}}$. One might be tempted to just skip this step, obtain a full sample $\boldsymbol{\theta}_k$, and subsequently sample $\boldsymbol{\eta}_k$ using, for example, the re-updating strategy in Section 3.3. However, doing so will result in a collapsed Gibbs sampler that does not target the correct stationary distribution (Van Dyk and Park, 2008). It is therefore important that $\boldsymbol{\eta}_k^{\mathcal{I}}$ is sampled concurrently with $\boldsymbol{\theta}_k^{\mathcal{I}}$ although, as we discuss next, a re-updating of $\boldsymbol{\eta}_k$ is necessary in practice to improve convergence of the MCMC chains.

3.3 Re-updating the process coefficients for scale $k = 1, \dots, K$

When a block of $\boldsymbol{\eta}_k$ gets updated conditional on everything else it is pinned at its boundary, because $\boldsymbol{\eta}_k$ is locally smooth a priori and, in regions where data density is low, a posteriori as well. This results in slow mixing of the Markov chains. We address this issue by re-sampling each $\boldsymbol{\eta}_k$ in a separate Gibbs step.

For each $\boldsymbol{\eta}_k$ we tile the domain D into tiles so that each element of $\boldsymbol{\eta}_k$ is then associated with exactly one tile, specifically the tile in which the basis function it weights is a maximum. Each tile is no larger than what can be processed on a single node, and so will be associated with about r_{η_0} basis functions, as per the update of $\boldsymbol{\eta}_0$. The tiles must also be large enough such that the elements of $\boldsymbol{\eta}_k$ associated with any two non-contiguous tiles (i.e., tiles that do not share a common boundary) are conditionally independent given the elements of $\boldsymbol{\eta}_k$ associated with the other tiles. These tiles and their neighbours can be used to establish a supergraph made up of *blocks* of $\boldsymbol{\eta}_k$, where each block (corresponding to one tile) is conditionally independent of the rest given its neighbours. This supergraph is then coloured such that no two neighbouring blocks have the same colour; for point-referenced data this will require at most four colours. The colouring also corresponds to one on the tiles where no two tiles which share a common border have the same colour.

As in the joint updating of $(\boldsymbol{\eta}_k, \boldsymbol{\theta}_k)$, this colouring allows us to develop a parallel sampler for $\boldsymbol{\eta}_k$. Specifically, consider two blocks of $\boldsymbol{\eta}_k$ that are associated with two tiles, with indices given by \mathcal{T}_1 and \mathcal{T}_2 , respectively. When these two blocks are of the same colour, $\boldsymbol{\eta}_k^{\mathcal{T}_1} \perp\!\!\!\perp \boldsymbol{\eta}_k^{\mathcal{T}_2} \mid \boldsymbol{\eta}_k^{\text{rest}}$ according to the structural zeros of \mathbf{Q}_k . Let \mathcal{F}_1 be the data footprint of $\boldsymbol{\eta}_k^{\mathcal{T}_1}$. Similarly, let \mathcal{F}_2 be the data footprint of $\boldsymbol{\eta}_k^{\mathcal{T}_2}$. For point-referenced observations it is straightforward to see that $\mathcal{F}_1 \cap \mathcal{F}_2 = \emptyset$ so that we can partition \mathbf{Z} as $\{\mathbf{Z}^{\mathcal{F}_1}, \mathbf{Z}^{\mathcal{F}_2}, \mathbf{Z}^{\text{rest}}\}$. The relevant part of the DAG for $\boldsymbol{\eta}_k$ and \mathbf{Z} is therefore simply the top part of that in (12),

$$\begin{array}{ccccc}
 \mathbf{Z}^{\mathcal{F}_1} & & \mathbf{Z}^{\text{rest}} & & \mathbf{Z}^{\mathcal{F}_2} \\
 \uparrow & \swarrow & \uparrow & \swarrow & \uparrow \\
 \boldsymbol{\eta}_k^{\mathcal{T}_1} & \leftarrow & \boldsymbol{\eta}_k^{\text{rest}} & \rightarrow & \boldsymbol{\eta}_k^{\mathcal{T}_2}
 \end{array} \tag{14}$$

Reading from the DAG,

$$\boldsymbol{\eta}_k^{\mathcal{T}_1} \perp\!\!\!\perp \boldsymbol{\eta}_k^{\mathcal{T}_2} \mid \mathbf{Z}^{\mathcal{F}_1}, \mathbf{Z}^{\mathcal{F}_2}, \boldsymbol{\eta}_k^{\text{rest}}, \text{eelse}, \tag{15}$$

and therefore $\boldsymbol{\eta}_k^{\mathcal{T}_1}$ and $\boldsymbol{\eta}_k^{\mathcal{T}_2}$ can be updated in parallel (Wilkinson, 2006). The log of the full conditional distributions are identical in form to (8) with the same extra term mentioned in Section 3.2 which is simple to compute. Therefore each of these updates again requires only a small chunk of data, matrices, and subsets of samples of the other process coefficients, so that each of these updates can also be done via a distributed-data architecture .

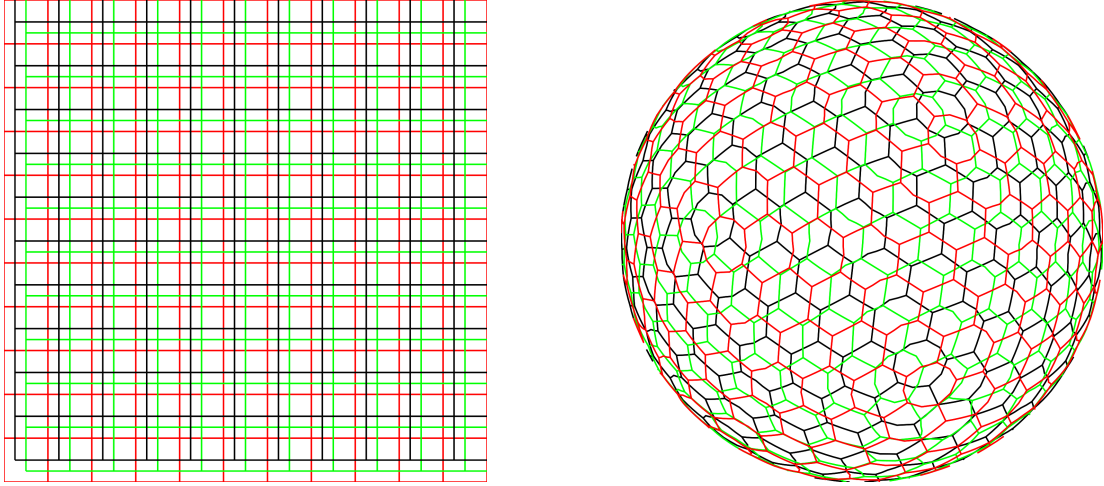


Figure 1: Example of three tilings on $D \subset \mathbb{R}^2$ (left panel) and $D = \mathbb{S}^2$ (right panel) that ensure that basis functions (not shown) are not in the vicinity of a boundary in at least one of the tiles.

Even though this sampling constitutes a re-update of $\boldsymbol{\eta}_k$, this coloured-tile scheme has got its own boundaries close to which the process coefficients will experience poor mixing. We address this by using three tilings for each k , one after another in the Gibbs sampler. Each tiling is shifted by about a third of a tile, relative to the one before. This ensures that no element of $\boldsymbol{\eta}_k$ is always near a boundary when Gibbs sampling. We show three such tilings on \mathbb{R}^2 and \mathbb{S}^2 in Figure 1. The resulting Gibbs sampler is an instance of a blocked sampler where the blocks are not disjoint; see, for example Jensen et al. (1995).

3.4 Updating the measurement-error variance parameters

Consider now the parameters $\boldsymbol{\theta}_\varepsilon$. The submodel for the Gibbs update of these parameters is made up of

$$\mathbf{Z} \mid \boldsymbol{\eta}, \boldsymbol{\theta}_\varepsilon \sim \text{Gau}(\mathbf{A}\boldsymbol{\eta}, \mathbf{D}), \quad (16)$$

and (3) with $X = \varepsilon$, where $\mathbf{D} \equiv \mathbf{Q}_\varepsilon^{-1}$ is diagonal with non-zero elements $\mathbf{D}_{ll} = (\mathbf{b}_\varepsilon(\mathbf{s}_l)^\top \boldsymbol{\theta}_\varepsilon)^2, l = 1, \dots, m$. As with $\boldsymbol{\eta}_k$ and $\boldsymbol{\theta}_k$, elements of $\boldsymbol{\theta}_\varepsilon$ are spatially-indexed by the maximum of the basis functions they weight. Let \mathcal{I} contain the index of one element of $\boldsymbol{\theta}_\varepsilon$. The data footprint \mathcal{F} of $\boldsymbol{\theta}_\varepsilon^{\mathcal{I}}$ contains the indices of the data points that lie in $\text{supp}(\mathbf{b}_\varepsilon^{\mathcal{I}})$. For two elements of $\boldsymbol{\theta}_\varepsilon$ with indices \mathcal{I}_1 and \mathcal{I}_2 , respectively, and for which $\mathcal{F}_1 \cap \mathcal{F}_2 = \emptyset$, the relevant part of the conditional independence graph is

$$\begin{array}{ccccc}
 \mathbf{Z}^{\mathcal{F}_1} & & \mathbf{Z}^{\text{rest}} & & \mathbf{Z}^{\mathcal{F}_2} \\
 \uparrow & \swarrow & \uparrow & \searrow & \uparrow \\
 \boldsymbol{\theta}_\varepsilon^{\mathcal{I}_1} & & \boldsymbol{\theta}_\varepsilon^{\text{rest}} & & \boldsymbol{\theta}_\varepsilon^{\mathcal{I}_2}
 \end{array} \quad (17)$$

because the components of \mathbf{Z} are independent given $\boldsymbol{\theta}_\varepsilon$ and everything else, and the components of $\boldsymbol{\theta}_\varepsilon$ are IID in the prior.

As with $\boldsymbol{\eta}_1$, the condition $\mathcal{F}_1 \cap \mathcal{F}_2 = \emptyset$ is essential, but this is easily satisfied in our context since $\mathbf{b}_\varepsilon(\cdot)$ are tent basis functions and the data are point-referenced. In

particular, this condition is satisfied whenever $\theta_\varepsilon^{I_1}$ and $\theta_\varepsilon^{I_2}$ are not neighbours in the graph implied by T_ε . In this case, the full conditional dependence graph of θ_ε is just an edge-preserving bijection of the spatial graph T_ε , with θ_ε as the vertices. We therefore also colour it using four colours and, noting that the DAG (17) has the same structure as (14), we use the same strategy of parallel updating parameters of the same colour. The full conditional distribution,

$$\text{pr}(\theta_\varepsilon^{I_1} \mid \text{eelse}) \propto \text{pr}(\mathbf{Z}^{\mathcal{F}_1} \mid \theta_\varepsilon^{I_1}, \theta_\varepsilon^{\text{rest}}, \boldsymbol{\eta}) \text{pr}(\theta_\varepsilon^{I_1}), \quad (18)$$

does not have a recognisable distribution, and so this update uses a Metropolis-Hastings step.

3.5 Summary of Gibbs sampler

Algorithm 1 gives a summary of all the stages in one complete pass through the Gibbs sampler. Each sample is generated conditional on \mathbf{Z} and the most recent samples of the other random variables, again denoted here as ‘eelse’ for ‘everything else.’ When the conditional distribution to sample from is not available in closed form, the update is done via an accept-reject step; in our application in Section 5 we use adaptive random walk Metropolis proposals. In Algorithm 1 we use the superscript $*$ to denote intermediate quantities: these quantities are discarded in the final output of the Gibbs sampler.

Algorithm 1: Parallel Gibbs Sampler

1. Sample $(\boldsymbol{\eta}_0, \boldsymbol{\theta}_0) \mid \text{eelse}$.
2. For $k = 1, \dots, K$
 - (a) Sample $(\boldsymbol{\eta}_k^*, \boldsymbol{\theta}_k) \mid \text{eelse}$ in parallel (≥ 4 colours).
 - (b) Sample $\boldsymbol{\eta}_k \mid \text{eelse}$ in parallel (4 colours).
3. Sample $\boldsymbol{\theta}_\varepsilon \mid \text{eelse}$ in parallel (4 colours).
4. Shift the tiling for each $\boldsymbol{\eta}_k, k \geq 1$, to the next position and go to step 1.

All steps in the Gibbs sampler use distributed-data and distributed-model updates, and all steps except for step 1 use parallel computation to obtain a complete sample in a fixed number of sweeps (usually 4). It is worth re-iterating that, despite the re-updating of $\boldsymbol{\eta}_k$ in step 2(b), updating $\boldsymbol{\eta}_k$ for each colour in step 2(a) is still required in order to ensure the correct stationary distribution is targeted when going through the colours in sequence (Van Dyk and Park, 2008).

4 Guidelines for constructing triangulations and prior distributions

The favourable computational properties of the updates in Section 3 can only be taken advantage of if sensible triangulations are used for the process and parameter decompositions. Further, the separation of $Y(\cdot)$ into separate scales introduces identifiability

concerns, akin to those seen in problems of spatial source separation (Nordhausen et al., 2015). Therefore, judicious construction of the triangulations and prior distributions on the length scales (that help to separate the scales in spectral space) are required. Our guidelines below are based on point-referenced observations that have relatively high signal-to-noise ratio; these guidelines may need to be slightly adjusted when this is not the case.

The key design criterion is the size of largest matrix that can be efficiently factorised on a single computing node. Using hardware and linear algebra libraries current as of the year 2019, sparse precision matrices of dimension 50000 constructed from a second-order GMRF on \mathbb{R}^2 (subject to appropriate fill-in reducing permutations) can be factorised extremely quickly on a single computing node. A regular triangulation T_{η_0} on D should therefore be constructed such that r_{η_0} is between 10^4 and 10^5 . The prior distribution on ρ_0 should reflect the average edge length in this triangulation; we suggest that a low percentile of $\text{pr}(\rho_0)$, the 2.5 percentile say, is no smaller than one to two times the average edge length in T_{η_0} . This choice is motivated by the Nyquist–Shannon criterion, which is also used for basis function placement by Zammit-Mangion et al. (2012). From a practical point of view, it encapsulates the fact that signal components with finer scales cannot be captured by this decomposition of $Y_0(\cdot)$ on T_{η_0} . The upper quantile can usually be set based on application considerations. The hyperparameters for $\text{pr}(\sigma_0)$ can be uninformative or set via exploratory data analysis.

At the other end of the spectrum, the finest triangulation should be fine enough so that the size of the data footprint associated with each element of $\boldsymbol{\eta}_K$ is small, and preferably in the single digits. This guideline ensures that our model is able to resolve the highest frequency components that may be extracted from the data. If we do not do this, then our predictions at the finest scale are possibly over-smoothed (i.e., the model is underfitting). The prior distribution of each element in $\boldsymbol{\theta}_{\rho_K}$ should again have a lower percentile that is no smaller than one to two times the average edge length in T_{η_K} . In a two-scale model ($K = 1$), the upper quantile should be set close to, but above, the lower 2.5 percentile of $\text{pr}(\rho_0)$, in order to ensure some spectral overlap between the scales. The number of scales to use is largely a modelling choice but is also determined by the span in spectral frequencies that can be captured by $Y_0(\cdot)$ and $Y_K(\cdot)$. A good rule of thumb is to ensure that the 95% highest prior density interval associated with each length scale spans one or two orders of magnitude. However, the choice of effective process footprints at each scale might further constrain the choice of prior distributions (see below), and thus the number of scales that are used. Since in this model source separation is done via the prior distributions of ρ_k , each $\text{pr}(\boldsymbol{\theta}_{\sigma_k}^{\{i\}})$ can be uninformative or identical to $\text{pr}(\sigma_0)$.

The coarseness or otherwise of the triangulation T_ε reflects a prior belief on how quickly (spatially) the measurement-error variance changes, and this choice is application-specific. The hyperparameters for $\text{pr}(\boldsymbol{\theta}_\varepsilon)$ are also application-specific. The triangulations T_{θ_k} on the other hand need to become finer with increasing k in such a way that the number of basis functions in $\mathbf{a}_k(\cdot)$ that have support intersecting $\mathbf{b}_k^\mathcal{I}(\cdot)$, for each \mathcal{I} , is on the order of r_{η_0} . This recursive refining of T_{θ_k} with k yields an attractive model where the degree of nonstationarity of the process increases with the scale k .

The effective process footprint of each $\boldsymbol{\theta}_k^\mathcal{I}$ is a design choice. In principle, the footprint needs to be one such that the approximation (11) is sensible for any values that are not in the tails of the prior distribution. For example, one might use a spatial buffer around $\text{supp}(\mathbf{b}_k^\mathcal{I})$ of width equal to the upper 97.5 percentile of the prior distribution $\text{pr}(\boldsymbol{\theta}_{\rho_k}^\mathcal{I})$ to define the effective process footprint of $\boldsymbol{\theta}_k^\mathcal{I}$. If this footprint is so large that sampling of

$\theta_k^{\mathcal{I}}$ becomes prohibitive, then tighter prior distributions (and hence more scales in order to ensure spectral coverage everywhere) would need to be used if this approximation is of concern. Alternatively, one may run a number of MCMC chains with different computationally inexpensive effective process footprints in parallel, and verify that the target distribution is indeed (approximately) independent of the chosen footprint size.

In a separate experiment we verified empirically that the total variation distance between the true conditional distribution $\text{pr}(\boldsymbol{\eta}_k^{\text{rest}} \mid \boldsymbol{\theta}_k^{\mathcal{I}}, \boldsymbol{\theta}_k^{\text{rest}})$ and $\text{pr}(\boldsymbol{\eta}_k^{\text{rest}} \mid \tilde{\boldsymbol{\theta}}_k^{\mathcal{I}}, \boldsymbol{\theta}_k^{\text{rest}})$ is negligible for a large range of $\boldsymbol{\theta}_k^{\mathcal{I}}$ and effective process footprints. We therefore believe that this approximation is not of any practical concern. As discussed in Section 3.2, in our application we have taken a minimal approach and used relatively small effective process footprints. This choice does not seem to have had a detrimental effect on the quality of the probabilistic predictions which, as we show in Section 5, are considerably better than those obtained from competing (simpler) models.

5 Case study: Spatial modelling and prediction of sea-surface temperature from VIIRS

A sophisticated distributed implementation on a multi-node cluster is required for the sampler to be used with data-set sizes on the order of tens or hundreds of millions and with models with many ($K > 1$) scales. However, a two-scale model with approximately one million basis functions and one million data points can be implemented on a standard multi-core (in our case a deca-core) desktop computer using a crude implementation in R (R Core Team, 2019), whereby the “chunks” required for each parallel sample (implemented via the function `mclapply`) are loaded from disk when needed. This data size is still considered fairly large in spatial analyses, and we therefore restrict ourselves to this case in this article. An implementation that allows for orders of magnitude more data and basis functions is being developed and will be discussed elsewhere.

We compare inferences from the two-scale variant of the multi-scale spatial process model with those from several other spatial models and approximation methods, specifically a coarse-scale SPDE model; a suite of independent fine-scale SPDE models over spatially contiguous blocks of data; a single-scale model approximated using a full-scale approximation (FSA); a stationary multi-scale process model constructed using a relatively small number of basis functions, and a single-scale process model using the approximations via a nearest-neighbour Gaussian process approximation. These models and approximations were chosen to show that several aspects of the proposed multi-scale model, namely the use of multiple scales, the use of a large number of basis functions, and the use of nonstationarity, are crucial to get good predictions in a typical big-data environmental spatial data analysis.

5.1 Data

As data we used global sea-surface temperature (SST) obtained from the Visible Infrared Imaging Radiometer Suite (VIIRS) on board the Suomi National Polar-orbiting Partnership (Suomi NPP) weather satellite on October 14 2014 (Cao et al., 2013). We sampled one million data points at random from the complete data set, intentionally leaving data out from an $8^\circ \times 8^\circ$ box centred at (155°W , 0°N) in the Pacific Ocean, and used these as observation/training data. We then sampled another one million data points at random

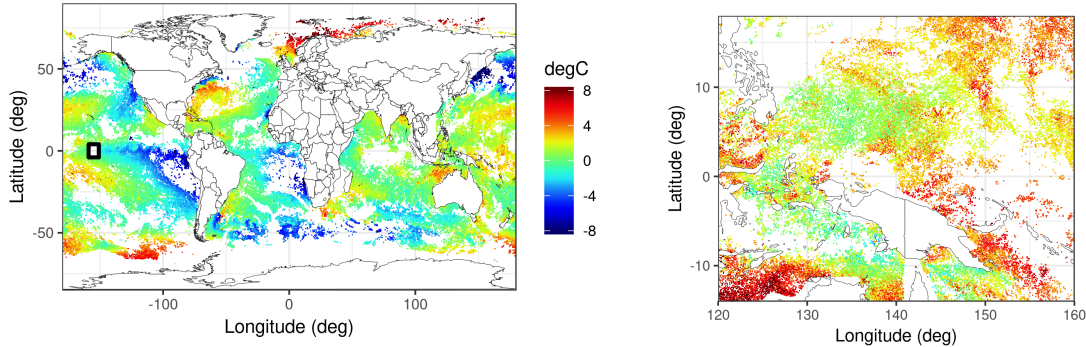


Figure 2: SST residuals used for training the model. (Left panel): Global view of residuals, with the $8^\circ \times 8^\circ$ box in the Pacific Ocean marked in black. Right panel: Residuals in an area of the Western Pacific around Papua New Guinea.

from the remainder and used these for assessing the quality of our predictions. After discarding obviously erroneous data, and data points that fell outside our constructed meshes (see Section 5.2) we were left with about 900000 data points in each of the training and validation data sets.

We then detrended the training and validation data sets by fitting to them a linear model with an intercept, the latitude coordinate, and the square of the latitude coordinate, as covariates. The residuals from the training data are what we call \mathbf{Z} in Section 2, while we denote the residuals from the validation data set as \mathbf{Z}_v . In Figure 2 we show the residuals \mathbf{Z} on the globe together with the $8^\circ \times 8^\circ$ box (left panel) and a zoomed-in view of these residuals around Papua New Guinea (right panel). We can see from the figure that the spatial data are very irregularly-sampled in space, and that the distance from anywhere in the ocean to the nearest data point can range from a few kms to thousands of kms. The data also reveal both large-scale and small-scale features that need to be modelled.

5.2 Model Setup

We constructed the Delaunay triangulations on \mathbb{S}^2 with rough boundary around land masses (used in a study by Simpson et al., 2016) using the mesher in INLA, and fixed $\nu_0 = \nu_1 = 1$. We determined the approximate number of vertices in the triangulations as follows, using the guidelines in Section 4. First, since it is required to factorise \mathbf{Q}_0 we made sure that T_{η_0} only contains a few tens of thousands of vertices, in our case it contains $r_{\eta_0} = 38274$ vertices. Second, since $Y_1(\cdot)$ models the small-scale variability and we are only considering two scales, we require T_{η_1} to be spatially dense with respect to the observed data. In our case we constructed a triangulation T_{η_1} with 942349 vertices. Using this triangulation the proportion of elements in $\boldsymbol{\eta}_1$ which have a data footprint size in the single digits is 92%. Finally, we want the nonstationarity in the fine-scale process to vary smoothly in space, and we therefore let $T_\varepsilon = T_{\theta_1}$ have only a few hundred vertices, in our case 205 vertices. Using this triangulation the largest effective process footprint is of size 27198, which is on the same order as r_{η_0} as desired. The triangulations on a small region of the Pacific Ocean are shown in Figure 3.

In order to re-sample $\boldsymbol{\eta}_1$ as discussed in Section 3.3, we constructed three partitionings of $\boldsymbol{\eta}_1$ from three spatial tilings of D . The first tiling was done using the third resolution of

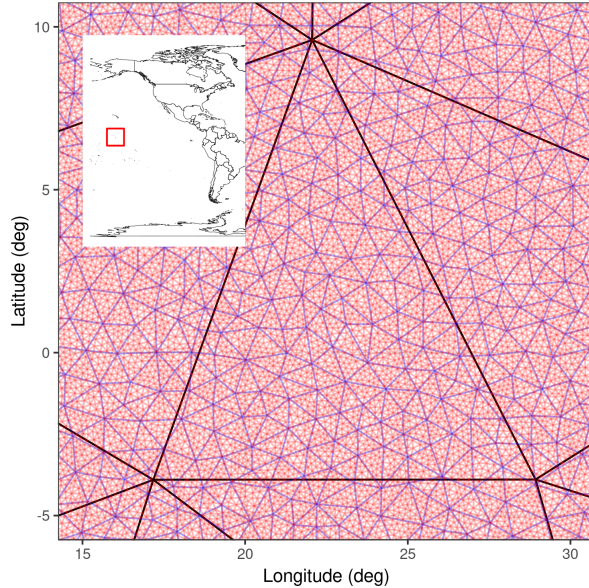


Figure 3: The triangulations T_{η_1} (red), T_{η_0} (blue), and T_{ε} ($= T_{\theta_1}$) (black) shown here for a small region in the Pacific Ocean as marked by the red rectangle in the inset.

an Icosahedral Snyder Equal Area Aperture 3 Hexagonal (ISEA3H) grid on the surface of the sphere. The second and third tilings were then done by shifting the ISEA3H grid north and east, respectively; see Figure 1, right panel. To improve mixing of the MCMC chains, spatial tiles that contained less than 100 data points or less than 200 basis functions at scale $k = 1$ were merged with neighbouring tiles. The three tilings and colourings are shown in Figure 4.

We constructed the prior distributions following the guidelines of Section 4. As prior distribution for ρ_0 we used a lognormal distribution such that $[\rho_{0,0.025}, \rho_{0,0.975}] = [300, 10000]$ km, where $\rho_{0,q}$ denotes the q th quantile of the distribution. Our choice of $\rho_{0,0.025}$ stems from us choosing a maximum edge length of 150 km when constructing T_{η_0} , while our choice of $\rho_{0,0.975}$ presents a soft maximum on what we believe the spatial correlations in SSTs are (10000 km equates to approximately half the greatest east-west span of the Pacific Ocean). On the other hand, as prior distribution for $\theta_{\rho_1}^{\{i\}}, i = 1, \dots, r_{\rho_1}$, we used a lognormal distribution such that $[\theta_{\rho_1,0.025}^{\{i\}}, \theta_{\rho_1,0.975}^{\{i\}}] = [30, 900]$. The lower quantile was selected on the basis that we used 30 km as our maximum edge size when constructing T_{η_1} , while the upper quantile was selected to ensure that there is sufficient spectral overlap between $Y_0(\cdot)$ and $Y_1(\cdot)$. As for the marginal process standard deviation, we used a lognormal distribution such that $[\sigma_{0,0.025}, \sigma_{0,0.975}] = [\theta_{\sigma_k,0.025}^{\{i\}}, \theta_{\sigma_k,0.975}^{\{i\}}] = [0.1, 6]^{\circ}\text{C}$, where our upper quantile was selected from the fact that the empirical standard deviation of the SST residuals is approximately equal to 2°C . Finally, as prior for the measurement error standard deviation we used a lognormal distribution such that $[\theta_{\varepsilon,0.025}^{\{i\}}, \theta_{\varepsilon,0.975}^{\{i\}}] = [0.5, 5]$, which reflects our prior belief that it is unlikely that the measurement error standard deviations are less than 0.5°C or larger than 5°C .

The Gibbs sampler algorithm in Section 3.5 was run for 10000 iterations. The first 5000 samples were discarded as burn-in and the remaining 5000 were thinned by a factor of 50, to yield 100 samples from the posterior distribution over all the states and parameters. It took approximately 5 days of computing time to obtain 10000 samples using our crude

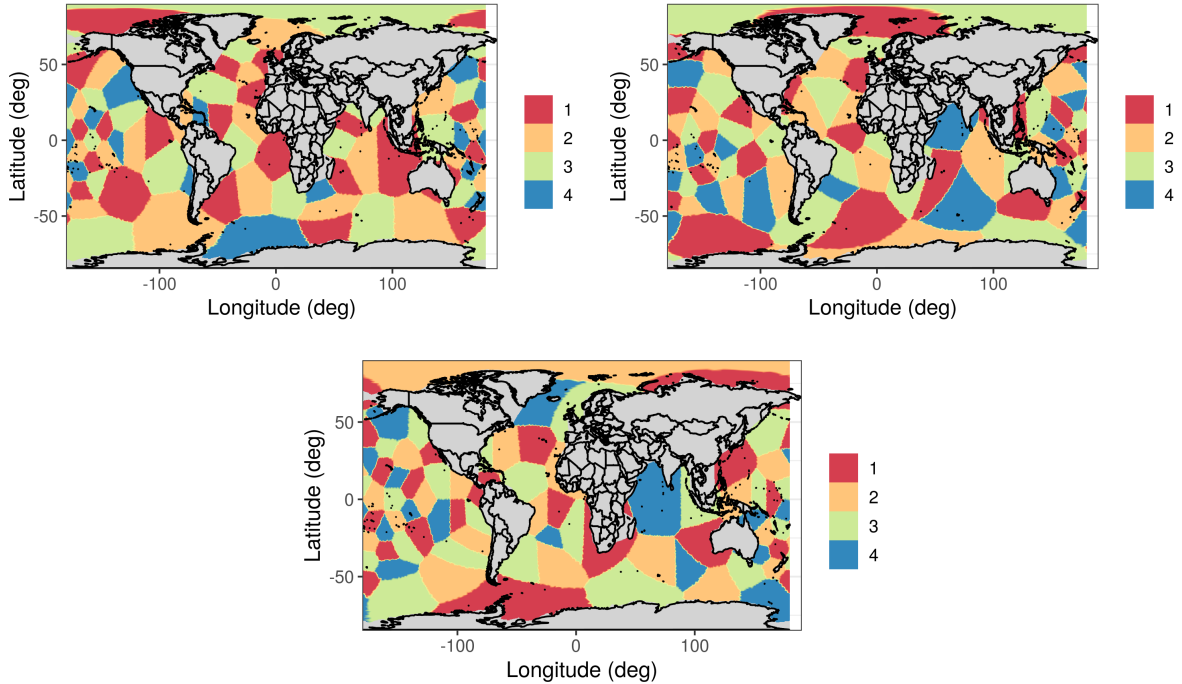


Figure 4: Colourings of the three tilings of η_1 .

implementation.

5.3 Other models

We compared the proposed model and its predictions (SPDE2) to several other models and approximations commonly used in applications containing large spatial data sets. We describe these in more detail below.

Global coarse-scale model (SPDE0): We used INLA to fit the SPDE (Lindgren et al., 2011) in (1) to the entire data set via a GMRF on the coefficients of the tent basis functions on T_{η_0} . We let $\nu = 1$ and used the same prior distributions for ρ_0 and σ_0 as we did for our two-scale spatial model in Section 5.2. We compare to this model to demonstrate the benefit of using a second, small-scale process when modelling such large spatial data sets. It took approximately 30 minutes of computing time to fit the model and obtain predictions with SPDE0.

Multiple spatially-independent small-scale processes (SPDE1-indep): We used INLA to independently fit SPDEs with spatially-invariant parameters to data that lie in each of the tiles shown in Figure 4, top-left panel. For each set of tile indices \mathcal{T} in our model SPDE2, we generated a fine-resolution mesh that has a similar number of basis functions as $|\mathcal{T}|$, and a few more around the boundary of the partition to reduce boundary effects. We let $\nu = 1$ and used the same prior distributions for (the now spatially-invariant) σ and ρ in each tile as we did for our two-scale process model in Section 5.2. These independent models were used to predict the noisy process at validation data locations that lie within their associated tile. Results from this model are used to

demonstrate the benefit of having a large-scale process that can borrow strength across large spatial scales when modelling large spatial data. It took approximately 6 hours to sequentially fit the models and obtain predictions with SPDE1.

Multi-scale stationary process with a relatively small number of basis functions via LatticeKrig (LTK): We used `LatticeKrig` (Nychka et al., 2015) to fit a 3-resolution LatticeKrig model on the cylinder (modelling on the sphere with over 100000 basis functions was prohibitively slow) comprising of a total of 137577 basis functions. Note that many of these basis functions (approximately one third) are over land. We fitted three LTK models with the parameter `a.wght`, which dictates the spatial range, fixed to 4.01, 5.01, and 6.01, respectively. In Section 5.4 we only show results for the case `a.wght = 6.01`, which provided slightly better predictions than the other two cases (all cases gave very similar predictions). LTK models are generally limited to $r = 100000$ to 200000 basis functions since they require factorisation of precision matrices of dimension $r \times r$ when being fit. Results from this model are used to demonstrate that hundreds of thousands of basis functions are still likely to be insufficient when modelling very large-scale data, despite using multi-scale process models. Fitting and predicting (via 30 conditional simulations) with LTK required approximately one day of computing time.

Single-scale process approximated using a full-scale approximation (FSA): The full-scale approximation (Sang and Huang, 2012) to a Matérn covariance function with smoothness $\nu = 1$ was implemented on \mathbb{R}^2 using 100 knots randomly placed on the surface of the sphere before projection onto the plane. The number of blocks on which to approximate the residual field was set to 9000 and data were attributed to each of these blocks using a k-means clustering algorithm on the lon-lat coordinates of the data. This choice ensured that the number of data points in each block was computationally feasible at about 100 data points per block. It took approximately two days to fit and predict using the FSA.

Single-scale process approximated using nearest neighbours (NNGP): We used the R package `spNNGP` to implement a conjugate version of the nearest-neighbour Gaussian process (NNGP, Finley et al., 2019), where several NNGPs are fitted for several plausible values of the latent-process range and variance, and cross-validation is used to select the best of these models for prediction. In each of these models an inverse-gamma prior distribution is used for the observation measurement-error variance, which yields closed-form predictive distributions that are quick to evaluate. In our implementation we set the number of neighbours to 15, the covariance function to a Matérn covariance function with $\nu = 1$, and used a fine grid for the latent-process range and variance, ensuring that an interior point of this grid was selected as optimal. It took approximately three hours to find the optimal NNGP model through cross-validation and to predict using the optimal model.

Results from the FSA and NNGP are used to show that fast approximations to single-scale process models that are done in such a way so as to reproduce process fine scales are not competitive against models like SPDE2 which are able to borrow strength across large spatial scales when predicting over large gaps.

5.4 Results

In Figure 5 we show predictions (posterior means) and prediction standard errors for $Y(\cdot)$ (top) using the two-scale spatial-process model SPDE2. The detail in these maps is very high – the one million basis functions effectively model the SST at a 30×30 km resolution globally. The posterior expectations of the parameters θ_ε , θ_{σ_1} and θ_{ρ_1} varied considerably. In particular, $E(\log \theta_\varepsilon \mid \mathbf{Z})$ ranged between -3.1 and 2.4 ; $E(\log \theta_{\sigma_1} \mid \mathbf{Z})$ ranged between -3.0 and 3.7 ; and $E(\log \theta_{\rho_1} \mid \mathbf{Z})$ ranged between -9.9 and 0.1 . This suggests that there is ample nonstationarity at small scales that is being captured by SPDE2.

We compare the predictions from all the models in terms of the root-mean-squared prediction error (RMSPE), continuous-ranked probability score (CRPS), 90% interval score (IS90), and the 90% coverage (Cov90) at the validation-data locations. To assess the models’ ability to predict and quantify uncertainty correctly at validation-data locations that are in regions of both dense and sparse training data, we split the validation data set into three: $\mathbf{Z}_v^{(1)}$ contains all the validation data outside the $8^\circ \times 8^\circ$ box in the Pacific Ocean that are in the vicinity of training data (specifically, a $1^\circ \times 1^\circ$ box centred on each datum in $\mathbf{Z}_v^{(1)}$ contains at least one training datum within it); $\mathbf{Z}_v^{(2)}$, which contains the validation data not in the vicinity of training data and outside the $8^\circ \times 8^\circ$ box; and $\mathbf{Z}_v^{(3)}$ that contains the validation data within the $8^\circ \times 8^\circ$ box. The dimensions of $\mathbf{Z}_v^{(1)}$, $\mathbf{Z}_v^{(2)}$, and $\mathbf{Z}_v^{(3)}$ were 896680, 895, and 6964, respectively.

Diagnostics of the marginal prediction distributions from each model are provided in Tables 1–3. In Table 1 we show diagnostics for when prediction locations are in the vicinity of data points. As expected, the models that only model coarse scales and/or rely on a relatively small number of basis functions (SPDE0 and LTK) give relatively poor predictions. On the other hand, the use of a high number of basis functions (SPDE2 and SPDE1-indep) and the single-scale models that are able to reproduce the fine-scale process variation (FSA and NNGP) give good predictions. All methods give the correct coverage. What we deduce from these results is well-known: When doing spatial prediction on large data sets there is little benefit in using a global model when predicting at locations close to observed data (unless the signal-to-noise-ratio is very low; see, e.g., Zammit-Mangion et al., 2018) if the target of the spatial analysis is pointwise prediction. There is also likely to be little benefit to be gained from using nonstationary process models since the inferences are predominantly data-driven and not model-driven. Rather, it is crucial to use a latent process model that is able to reproduce the fine-scale variation in the underlying process.

In Table 2 we show diagnostics for when prediction locations are not in the vicinity (through the $1^\circ \times 1^\circ$ boxes described earlier) of observations. Now we start to see the benefit of using a multi-scale process model where both small and large scales can be simultaneously captured. The relative disparity to the models with relatively few basis functions (LTK and SPDE0) is now less, while FSA and NNGP begin to give poorer predictions. The latter was expected; both these models estimated spatial range parameters that were small, rendering them useful in predicting at small scales, but not at large scales. Finally, in Table 3 we show predictions for validation data inside the $8^\circ \times 8^\circ$ lon-lat box. Here the single scale/fine-scale methods perform considerably worse than the global (SPDE0 and LTK) models that are able to borrow strength across large spatial scales. These, however, still do not perform well on the boundary of the lon-lat box where borrowing of strength across small scales is possible. The two-scale model out-

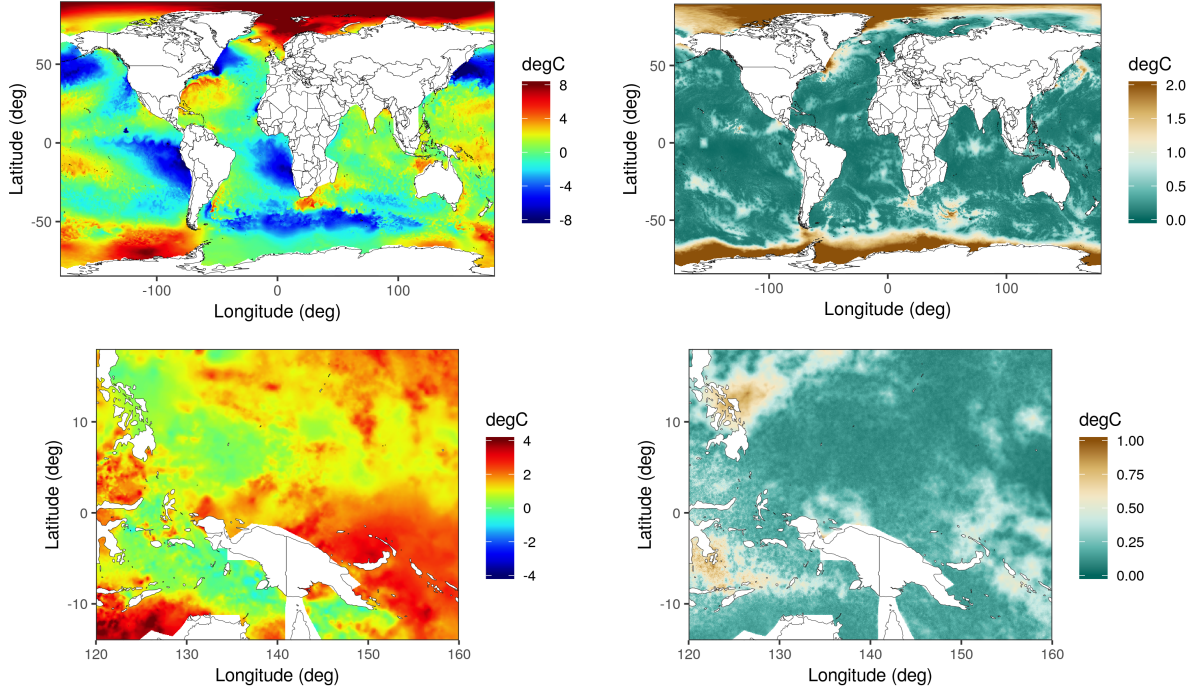


Figure 5: Global predictions (posterior means, top-left panel) and prediction standard errors (top-right panel) of $Y(\cdot)$ from the two-scale spatial-process model (SPDE2) when fitted to the data shown in Figure 2, left panel. Predictions and prediction standard errors corresponding to the region depicted in Figure 2, right panel, are shown in the bottom-left and bottom-right panels, respectively.

Table 1: Diagnostic results on the validation data $\mathbf{Z}_v^{(1)}$ (validation data in the vicinity of training data).

Model	RMSPE	CRPS	IS90	Cov90
FSA	0.125	0.185	1.659	0.915
LTK	0.143	0.200	1.752	0.913
NNGP	0.119	0.180	1.633	0.913
SPDE0	0.165	0.216	1.889	0.922
SPDE1-indep	0.120	0.180	1.557	0.919
SPDE2	0.119	0.176	1.479	0.907

performs the others by quite some margin in terms of RMSPE and CRPS. Interestingly all models except SPDE1-indep, and to a lesser extent SPDE2, are largely underconfident over this unobserved area.

6 Conclusion

The majority of models and inference techniques developed for analysing massive spatial data sets are not designed to model the multi-scale, nonstationary nature of the underlying process. The result is the widespread use of models that are able to provide good

Table 2: Diagnostic results on the validation data $\mathbf{Z}_v^{(2)}$ (validation data not in the vicinity of training data).

Model	RMSPE	CRPS	IS90	Cov90
FSA	0.190	0.217	1.946	0.921
LTK	0.183	0.223	1.953	0.914
NNGP	0.162	0.206	1.926	0.927
SPDE0	0.184	0.230	1.979	0.916
SPDE1-indep	0.156	0.198	1.719	0.932
SPDE2	0.147	0.191	1.543	0.928

Table 3: Diagnostic results on the validation data $\mathbf{Z}_v^{(3)}$ (validation data in the $8^\circ \times 8^\circ$ box).

Model	RMSPE	CRPS	IS90	Cov90
FSA	0.211	0.325	3.570	0.993
LTK	0.214	0.339	3.748	0.986
NNGP	0.265	0.422	5.000	0.996
SPDE0	0.181	0.282	2.926	0.995
SPDE1-indep	0.213	0.252	1.830	0.916
SPDE2	0.141	0.215	1.835	0.950

predictions at the fine scale (e.g., NNGP) or at the coarse scale when the number of basis functions for decomposition is capped for computational reasons. In this article we have proposed a multi-scale model where the degree of nonstationarity increases with the scale of the component processes, together with an approximate inference algorithm that is scalable with both data and model size. We have shown that it outperforms other state-of-the-art approaches that are amenable to big data scenarios, but that are unable to capture the complexities of the underlying process due to either the use of a few basis functions, or the use of a (typically) single scale to model the entire process. We conclude that multi-scale process models are essential for accurate modelling and prediction in environmental applications such as the analysis of SST, as is the ability to model non-stationarity and a computational strategy that allows for as many basis functions as one needs to reproduce the process' fine-scale components.

There are several avenues for future work. First, while the approximation (11) is a sensible one under the guidelines of Section 4, we do not provide any theoretical bound on the effect of the approximation on the target distribution, which is not straightforward to derive. Second, while our implementation in Section 5 used chunked-up data and models when doing inference, these were saved and loaded to disk when sampling via graph colouring. Sophisticated implementations include one where static objects (e.g., data and basis-function matrices) reside permanently in memory on dedicated nodes (Katzfuss and Hammerling, 2017), while communication of selected samples between the nodes is done efficiently via message passing (e.g., using MPI). Such an implementation would speed up the Gibbs sampler, and is necessary for the consideration of higher scales and data sets that are one to two orders of magnitude larger than that considered in Section 5. Third, there is considerable interest in making inference with large *non-Gaussian* spatial data.

Parallelisation is still possible for this case, but our computational framework would need to be modified slightly since the process coefficients cannot be sampled directly when the data is non-Gaussian. Specifically, when carrying out an update corresponding to a colour, the process coefficients would have to be proposed and then accepted or rejected jointly with the parameter coefficients; see, for example, Knorr-Held and Rue (2002).

Acknowledgements

We thank Yulija Marchetti for providing the sea-surface temperature data set, Bohai Zhang for providing the MATLAB code for the implementation of the FSA, Matt Moores for general discussions on improving MCMC mixing, and Quan Vu for providing comments on an early version of this manuscript. AZM was supported by an Australian Research Council (ARC) Discovery Early Career Research Award, DE180100203.

References

- Banerjee, S., Gelfand, A. E., Finley, A. O., and Sang, H. (2008). Gaussian predictive process models for large spatial data sets. *Journal of the Royal Statistical Society: Series B*, 70:825–848.
- Bender, E. A. and Wilf, H. S. (1985). A theoretical analysis of backtracking in the graph coloring problem. *Journal of Algorithms*, 6:275–282.
- Berliner, L. M. (1996). Hierarchical Bayesian time series models. In Hanson, K. M. and Silver, R. N., editors, *Maximum Entropy and Bayesian Methods*, pages 15–22. Springer, New York, NY.
- Cao, C., Xiong, J., Blonski, S., Liu, Q., Uprety, S., Shao, X., Bai, Y., and Weng, F. (2013). Suomi NPP VIIRS sensor data record verification, validation, and long-term performance monitoring. *Journal of Geophysical Research: Atmospheres*, 118:11664–11678.
- Cressie, N. and Johannesson, G. (2008). Fixed rank kriging for very large spatial data sets. *Journal of the Royal Statistical Society: Series B*, 70:209–226.
- Cressie, N. and Wikle, C. K. (2011). *Statistics for Spatio-Temporal Data*. John Wiley and Sons, Hoboken, NJ.
- Datta, A., Banerjee, S., Finley, A. O., and Gelfand, A. E. (2016). Hierarchical nearest-neighbor Gaussian process models for large geostatistical datasets. *Journal of the American Statistical Association*, 111:800–812.
- Dewar, M., Scerri, K., and Kadiramanathan, V. (2009). Data-driven spatio-temporal modeling using the integro-difference equation. *IEEE Transactions on Signal Processing*, 57:83–91.
- Finley, A. O., Datta, A., Cook, B. C., Morton, D. C., Andersen, H. E., and Banerjee, S. (2019). Efficient algorithms for Bayesian nearest-neighbor Gaussian processes. *Journal of Computational and Graphical Statistics*, in press.

- Gonthier, G. (2008). Formal proof – the four-color theorem. *Notices of the AMS*, 55:1382–1393.
- Jensen, C. S., Kjærulff, U., and Kong, A. (1995). Blocking Gibbs sampling in very large probabilistic expert systems. *International Journal of Human-Computer Studies*, 42:647–666.
- Katzfuss, M. (2017). A multi-resolution approximation for massive spatial datasets. *Journal of the American Statistical Association*, 112:201–214.
- Katzfuss, M. and Hammerling, D. (2017). Parallel inference for massive distributed spatial data using low-rank models. *Statistics and Computing*, 27:363–375.
- Knorr-Held, L. and Rue, H. (2002). On block updating in Markov random field models for disease mapping. *Scandinavian Journal of Statistics*, 29:597–614.
- Lindgren, F. and Rue, H. (2015). Bayesian spatial modelling with R-INLA. *Journal of Statistical Software*, 63(19).
- Lindgren, F., Rue, H., and Lindström, J. (2011). An explicit link between Gaussian fields and Gaussian Markov random fields: the stochastic partial differential equation approach. *Journal of the Royal Statistical Society: Series B*, 73:423–498.
- Nordhausen, K., Oja, H., Filzmoser, P., and Reimann, C. (2015). Blind source separation for spatial compositional data. *Mathematical Geosciences*, 47:753–770.
- Nychka, D., Bandyopadhyay, S., Hammerling, D., Lindgren, F., and Sain, S. (2015). A multiresolution Gaussian process model for the analysis of large spatial datasets. *Journal of Computational and Graphical Statistics*, 24:579–599.
- R Core Team (2019). *R: A Language and Environment for Statistical Computing*. R Foundation for Statistical Computing, Vienna, Austria.
- Rue, H. and Held, L. (2005). *Gaussian Markov Random Fields: Theory and Applications*. Chapman and Hall/CRC Press, Boca Raton, FL.
- Rue, H. and Tjelmeland, H. (2002). Fitting Gaussian Markov random fields to Gaussian fields. *Scandinavian Journal of Statistics*, 29:31–49.
- Sahu, S. K. and Mardia, K. V. (2005). A Bayesian kriged Kalman model for short-term forecasting of air pollution levels. *Journal of the Royal Statistical Society: Series C*, 54:223–244.
- Sang, H. and Huang, J. Z. (2012). A full scale approximation of covariance functions for large spatial data sets. *Journal of the Royal Statistical Society: Series B*, 74(1):111–132.
- Simpson, D., Illian, J. B., Lindgren, F., Srbye, S. H., and Rue, H. (2016). Going off grid: computationally efficient inference for log-Gaussian Cox processes. *Biometrika*, 103:49–70.
- Van Dyk, D. A. and Park, T. (2008). Partially collapsed Gibbs samplers: Theory and methods. *Journal of the American Statistical Association*, 103:790–796.

- Wikle, C. K., Zammit-Mangion, A., and Cressie, N. (2019). *Spatio-Temporal Statistics with R*. Chapman & Hall/CRC, Boca Raton, FL.
- Wilkinson, D. J. (2006). Parallel Bayesian computation. In Kontoghiorghes, E. J., editor, *Handbook of Parallel Computation and Statistics*, pages 477–508. CRC Press: Boca Raton, FL.
- Zammit-Mangion, A. and Cressie, N. (2019). FRK: An R package for spatial and spatio-temporal prediction with large datasets. *Journal of Statistical Software*, in press.
- Zammit-Mangion, A., Cressie, N., and Shumack, C. (2018). On statistical approaches to generate Level 3 products from satellite remote sensing retrievals. *Remote Sensing*, 10:155.
- Zammit-Mangion, A., Sanguinetti, G., and Kadiramanathan, V. (2012). Variational estimation in spatiotemporal systems from continuous and point-process observations. *IEEE Transactions on Signal Processing*, 60:3449–3459.